

Borehole breakouts

Authors: Dipl.-Ing. Rana Ammad Bin Sadiq & Prof. Dr. habil. Heinz Konietzky
(TU Bergakademie Freiberg, Geotechnical Institute)

1	Introduction.....	2
2	Mechanism of borehole breakout	2
3	Borehole breakout measurements	6
4	Borehole breakouts as stress indicators.....	7
5	Modes of Failure in a borehole	7
5.1	Borehole shear failure	7
5.2	Borehole tensile failure	9
6	Micro-mechanism of borehole breakout in different rocks	10
6.1	Borehole breakout in granite	10
6.2	Borehole breakout in limestone	12
6.3	Borehole breakout in highly porous and quartz-rich sandstone	13
7	Rock strength anisotropy and borehole breakouts	15
8	Estimating σ_{Hmax} from breakout.....	16
9	Numerical modeling of borehole breakout.....	19
10	Nomenclature	23
11	References	23

1 Introduction

Many researchers such as Leeman (1964) and Cox (1970) have reported the phenomenon of borehole elongation (borehole breakout), however, Bell and Gough in 1979 were the ones who received the most appreciation. They — during the study of an oil field in Alberta — observed that cross-sections of many deep boreholes elongate in NW-SE direction. They further explored this phenomenon and discovered that the elongations occurred at an angle of 90° from the direction of maximum far-field stress (σ_{Hmax}). Consequently, they suggested that occurrence of these borehole elongations offers clues about the direction of stresses within the earth. They called these elongations ‘borehole breakouts’. The idea to determine the direction and magnitude of the stresses based on borehole breakout analysis was further supported by many other researchers such as Plumb & Hickman (1985). In recent years, this technique has been successfully applied to many areas like petroleum engineering (e.g. Aslannezhad et al. 2016; Awal et al. 2001), deep geothermal energy (e.g. Shen, 2008) and in the study of reservoirs and repositories (David and Le Ravalec-Dupin, 2007).

2 Mechanism of borehole breakout

The stress concentration around a vertical well drilled parallel to the vertical principal stress (σ_v) in an isotropic, elastic medium is described by the Kirsch equations (Kirsch 1898). Kirsch illustrated that in a cylindrical opening (like a borehole) the stress trajectories tend to align themselves parallel and perpendicular to the walls of the wellbore, as shown in fig. 1.

The figure also shows the accumulation of stress trajectories at the azimuth of σ_{hmin} indicating strong compressive stress. On the other hand, the spreading out of stress trajectories at the azimuth of σ_{Hmax} indicate a stress reduction (trend toward tensile stresses). Before a wellbore is drilled, the rock is in a state of equilibrium and stresses in the earth under these conditions are known as far-field stresses or virgin in-situ stresses represented as σ_v , σ_{Hmax} and σ_{hmin} , as shown in fig. 2. Generally, these stresses are unequal (Haimson, 2007).

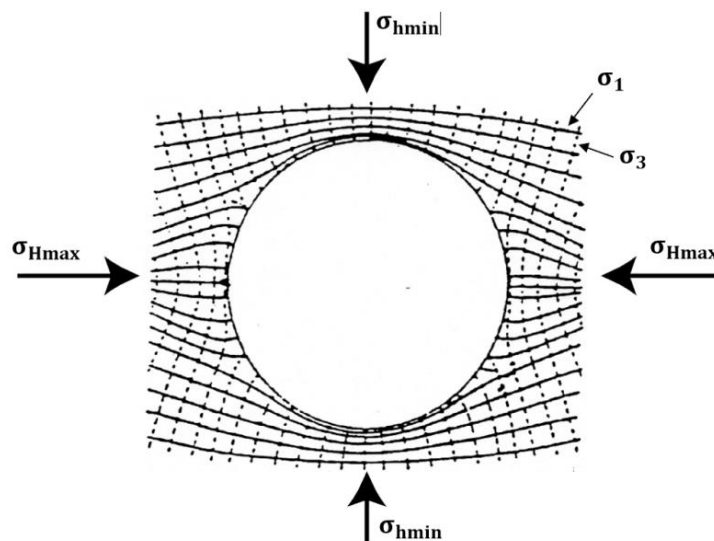


Fig. 1: Principal stresses around a cylindrical opening in a bi-axial stress field (Zoback, 2007)

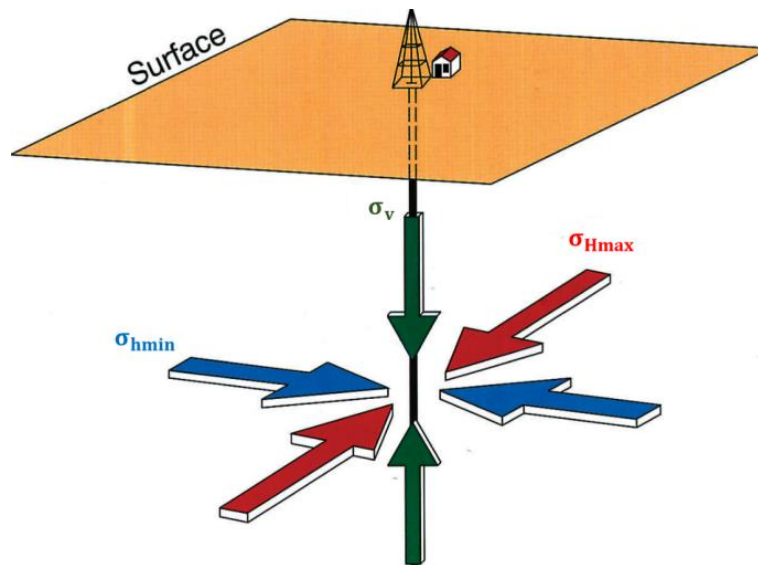


Fig. 2: Orientation of the principal stresses around a borehole (Bell et al. 1994).

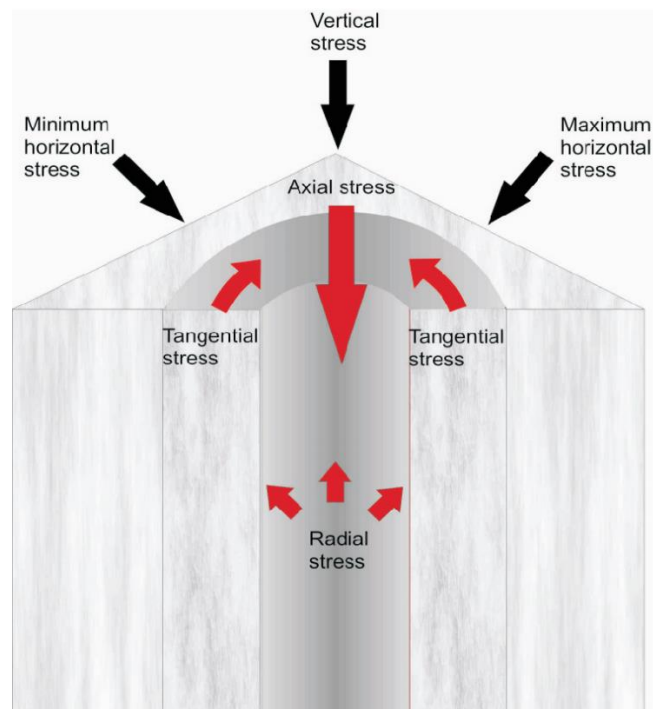


Fig. 3: Stresses around a borehole (Pašić et al., 2007).

The redistributed stresses around a borehole can also be expressed in cylindrical coordinates, in terms of radial stress σ_{rr} , tangential stress (also known as circumferential or hoop stress) $\sigma_{\theta\theta}$, and axial stress σ_a (see fig. 3). The radial stress acts in all directions perpendicular to the wellbore wall, the tangential stress circles the borehole, and the axial stress acts parallel to the wellbore axis, as shown in Fig. 3. If this redistributed stress state exceeds the rock strength - either in tension or compression - the rock fails (McLean and Addis, 1990). Mathematically, the effective stresses around a vertical wellbore of radius R are described in terms of a cylindrical coordinate system by the equations (1)-(3).

$$\sigma_{rr} = \frac{1}{2}(\sigma_{Hmax} + \sigma_{hmin}) \cdot \left(1 + \frac{R^2}{r^2}\right) + \frac{1}{2}(\sigma_{Hmax} + \sigma_{hmin}) \cdot \left(1 - \frac{4R^2}{r^2} + \frac{3R^4}{r^4}\right) \cos(2\theta) \quad (1)$$

$$\sigma_{\theta\theta} = \frac{1}{2}(\sigma_{Hmax} + \sigma_{hmin}) \cdot \left(1 + \frac{R^2}{r^2}\right) - \frac{1}{2}(\sigma_{Hmax} - \sigma_{hmin}) \cdot \left(1 + \frac{3R^4}{r^4}\right) \cos(2\theta) \quad (2)$$

$$\tau_{r\theta} = \frac{1}{2}(\sigma_{Hmax} + \sigma_{hmin}) \cdot \left(1 + \frac{2R^2}{r^2} - \frac{3R^4}{r^4}\right) \sin(2\theta) \quad (3)$$

where R is the radius of the borehole, r is the distance of the point from the centre of the borehole, and θ is measured from the azimuth of σ_{Hmax} .

Rock failure in compression is known as borehole breakout and failure in tension is known as induced (drilling or hydraulic) fracturing. In order to visualize the occurrence of breakouts and tensile fractures around a wellbore and to understand why these are such good indicators for far-field stress directions, the above equations for the stresses acting right at the wellbore wall are simplified by substituting $r = R$. In this case, the effective hoop stress $\sigma_{\theta\theta}$ and radial stress σ_{rr} at the wellbore wall are given by the following equations:

$$\sigma_{\theta\theta} = \sigma_{hmin} + \sigma_{Hmax} - 2(\sigma_{Hmax} - \sigma_{hmin}) \cos(2\theta) - P_0 \quad (4)$$

$$\sigma_{rr} = P_0 \quad (5)$$

where P_0 is the hydraulic borehole pressure.

The effective axial stress acting parallel to the wellbore axis is:

$$\sigma_a = \sigma_v - 2\nu(\sigma_{Hmax} - \sigma_{hmin}) \cos(2\theta) \quad (6)$$

where ν is Poisson's ratio.

For the location of minimum compression around the wellbore (i.e. parallel to σ_{hmin}) at $\theta = 0^\circ$ and $\theta = 180^\circ$, and the location of maximum stress concentration around the wellbore (i.e. parallel to σ_{Hmax}) at $\theta = 90^\circ$ and $\theta = 270^\circ$, equation (4) reduces to equations (7) and (8), respectively.

$$\sigma_{\theta\theta}^{\min} = 3\sigma_{hmin} - \sigma_{Hmax} - P_0 \quad (7)$$

$$\sigma_{\theta\theta}^{\max} = 3\sigma_{Hmax} - \sigma_{hmin} - P_0 \quad (8)$$

Subtracting eq. (8) from (7) leads to the following expression:

$$\sigma_{\theta\theta}^{\max} - \sigma_{\theta\theta}^{\min} = 4(\sigma_{Hmax} - \sigma_{hmin}) \quad (9)$$

Equation (9) shows that the stress difference between the maximum and the minimum value at the borehole wall is four times the difference between σ_{Hmax} and σ_{hmin} . Note that the stress components described in equation (9) are independent of the elastic moduli. For this reason, the above given equations do not vary from formation to formation. Moreover, the stress concentration around a wellbore is independent of R , rather the tangential stress depends on the magnitude of σ_{Hmax} , σ_{hmin} and P_0 . It is worth mentioning that as the distance from the wall of the borehole increases, these secondary stresses vanish rapidly and ultimately convert to the natural far-field stresses where the rock is in an undisturbed state.

If the strength of the rock is lower than the stresses accumulated, the rock will fail. Hence, if either compressive or tensile failure is going to occur, it will initiate at the borehole wall. Fig. 4(a) shows the numerical simulation of the evolution of borehole breakouts and the tensile failure around a borehole in an anisotropic stress field. Note, that the breakouts (indicated by the red crosses) appear on both sides of the borehole and tensile fractures (indicated by dark purple circles) develop perpendicular to the breakouts. As the breakout develops, its width remains unchanged but its depth increases gradually. The primary reason for this behaviour is the decrease in circumferential stresses after failure, which prevents further widening of the breakouts. Therefore with time, the width of the breakout does not change (Zoback et al., 1985). This feature is very important for the determination of stress conditions around the borehole, especially for the determination of direction and magnitude of σ_{Hmax} , which is discussed in section 8 below. Fig. 4(b) shows a real picture of a borehole breakout observed in the laboratory. Note, that breakouts are produced perpendicular to σ_{Hmax} .

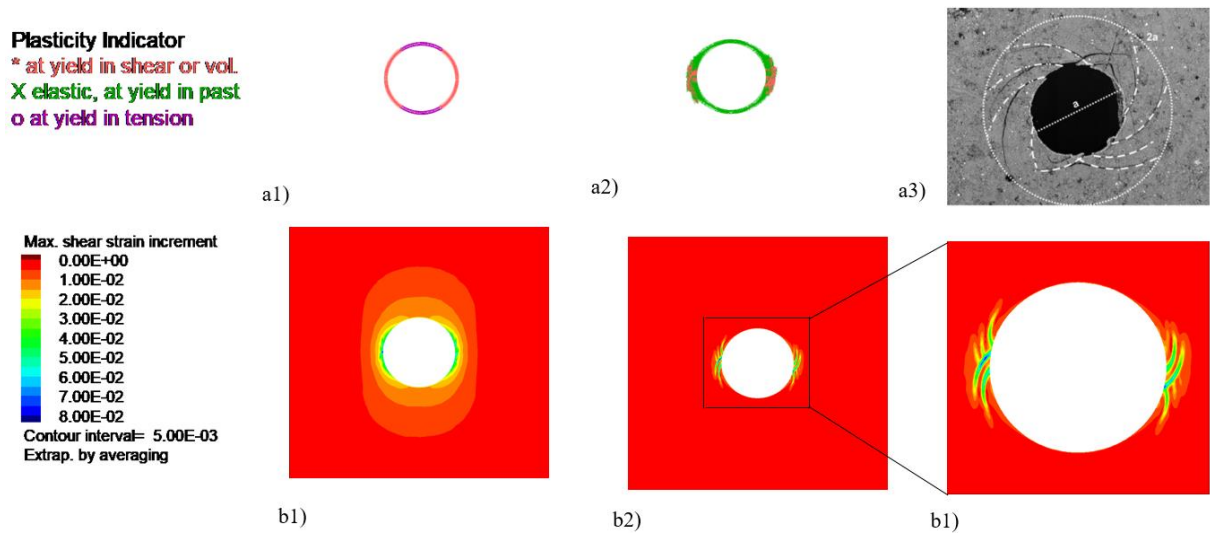


Fig 4: a) Illustration of the initial stage (a1 & b1) and stable borehole breakout (a2 & b2) in terms of plastic state and shear strain (Sadiq & Konietzky, 2018). Dark purple circles represent tensile failure, red crosses show active shear failure and green cross show elastic state. a3 & b3 comparison between borehole breakout observed in a laboratory experiment with simulation (Meier et al., 2013)

3 Borehole breakout measurements

Traditionally, the four-arm caliper is used to determine the orientation of breakouts. In this technique, the diameter of the borehole is continuously measured against the depth. The inclination and orientation of the tools are usually provided by a combination of north sensing magnetometer, gyroscope, and accelerometer. Fig. 5 shows data of a four-arm caliper for gauging hole and different modes of common failures (breakouts, washouts and key seats) in boreholes. When the pads of the instrument encounter breakout, two arms of the instrument expand, recording the increase in diameter on log reading, and the other two arms show the original unchanged diameter of the borehole as shown in figure 5(b) where the two arms of C1 measure the diameter of the borehole larger than the original. Because the sensitivity of this technique is low, one can confuse the breakout with other types of borehole failures such as washout and key seat. But with sufficient care, it is possible to use this technique to determine the breakout orientation. Townend & Zoback (2004) successfully used this technique to determine the stress orientations of coastal ranges of California. Electrical image logging tools and ultrasonic televiewer images also provide an accurate measure of borehole breakouts. These tools provide a 360° view of the borehole wall that allows for easy additional measurements of the breakout geometry, such as the azimuth and width of the breakout. These tools work in a manner similar to the four-arm caliper tool but additionally, provide high-resolution images. Breakouts in ultrasonic televiewer image appear as dark bands on either side of a well because of the low-amplitude ultrasonic reflections of the wellbore wall. Whereas in electrical image data, breakouts appear as out-of-focus areas because of the poor contact of the electrode arrays on the pads of the tool where breakouts are present (Asquith & Krygowski, 2004). Fig. 6 shows breakouts as identified by the dark bands (in ultrasonic images) and out of focus areas (in electrical images). With the help of these tools, a cross-sectional view of a well with breakouts can be easily prepared to show the azimuth of the breakouts and width of the breakout (fig. 6(c)).

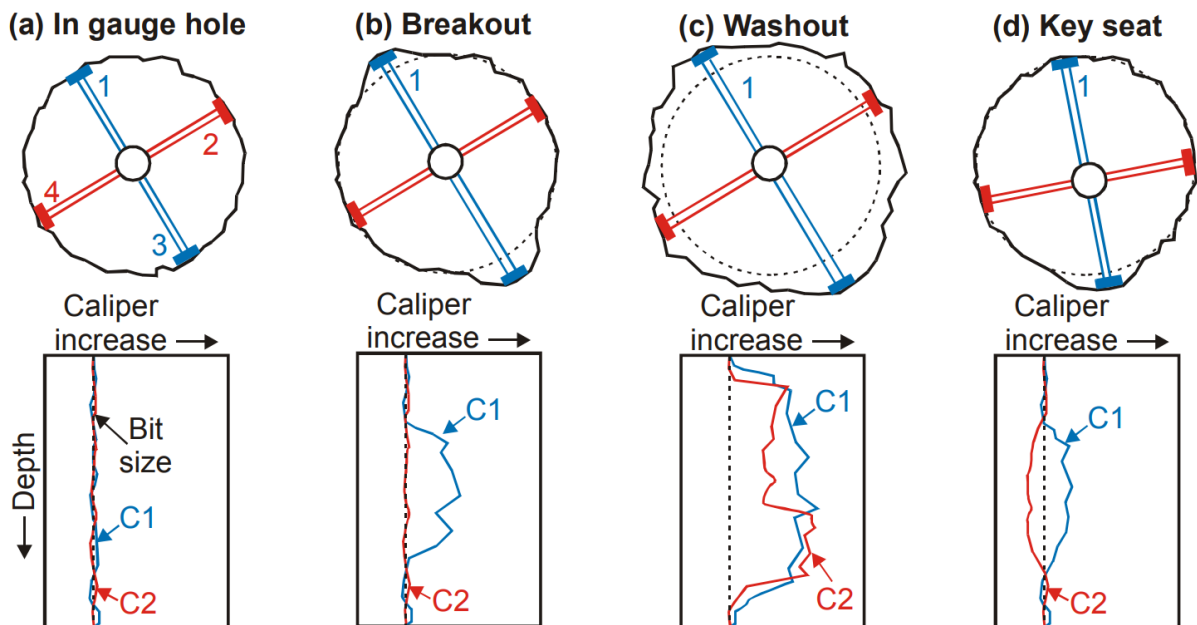


Fig. 5: Examples of four arm caliper data for the identification of different borehole geometries (Reinecker et al., 2003)

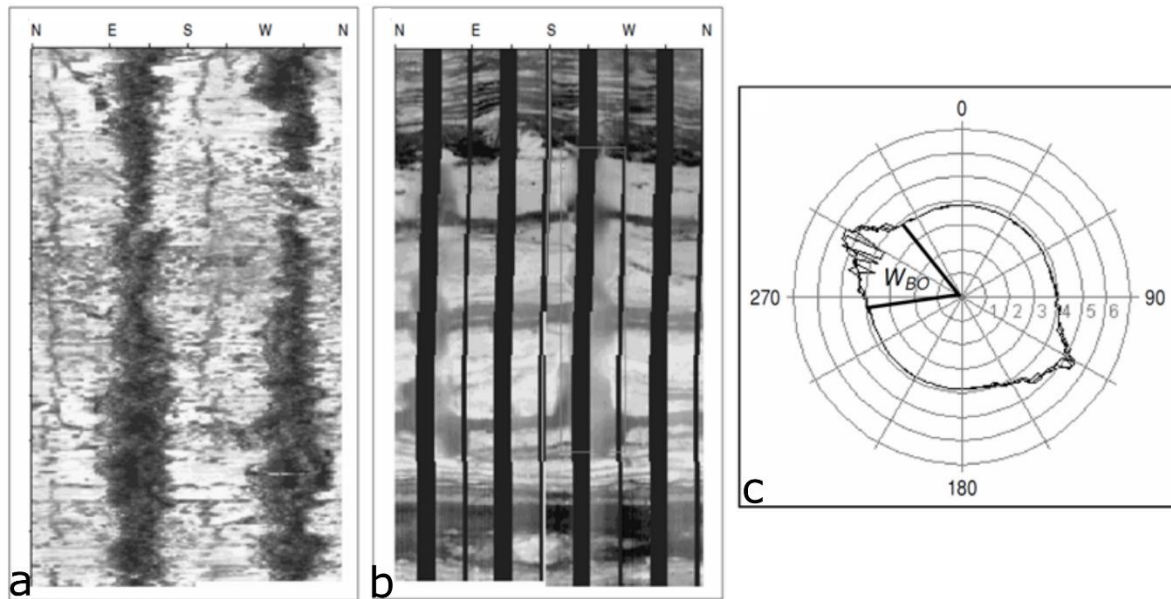


Fig. 6: (a) Resistivity log and (b) ultrasonic borehole televiewer image showing borehole breakouts. (c) A cross-sectional view of the borehole with breakouts (Zoback, 2007).

4 Borehole breakouts as stress indicators

Numerous studies in different parts of the world (e.g. Bell & Babcock, 1986; Klein & Barr, 1986; Plumb & Cox, 1987; Mount & Suppe, 1987; Zoback et al., 2003; Townend & Zoback, 2004) have shown that breakout orientations show remarkable consistency in a given well or in a given oil-field, and yield reliable measurements of stress orientation. The stress field construction by borehole breakouts is so reliable that it is an integral part of the World Stress Map Project (Zoback, 1992). Approximately 20 % of the World Stress Map (WSM) data were obtained from such methods (Bird, 2003) and their contribution to the WSM database is growing (Heidbach et al., 2010; Tingay et al., 2005).

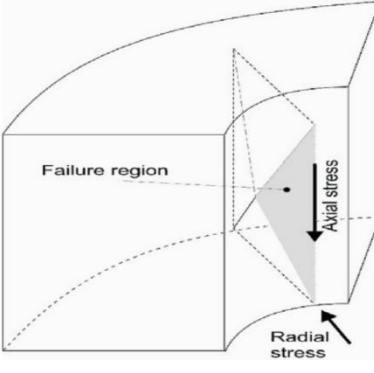
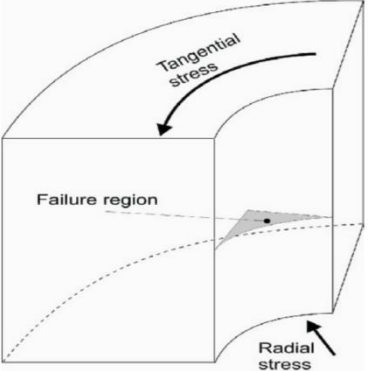
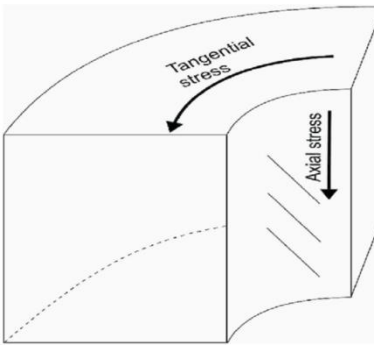
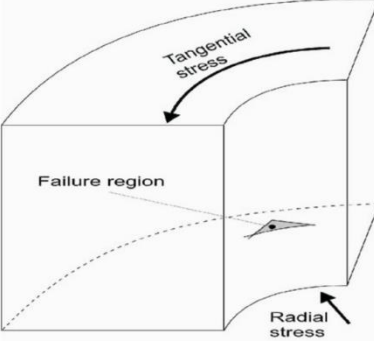
5 Modes of Failure in a borehole

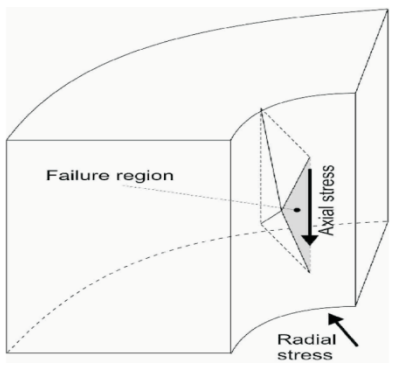
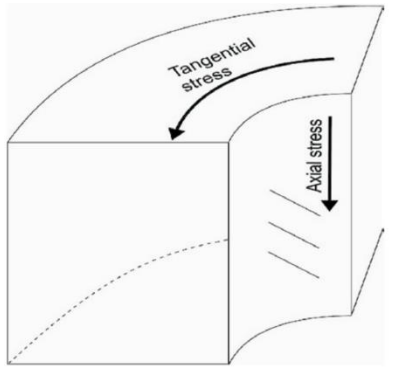
In boreholes, two basic modes of failure can be distinguished as shear failure and tensile failure.

5.1 Borehole shear failure

Bratton et al. (1999) pointed out that there are many types of breakouts. Tab. 1 and tab. 2 summarize six possible modes of shear wellbore failure and three possible modes of tensile failure, respectively.

Tab. 1. Modes of shear failure in rocks (after Pašić et al., 2007)

Failure type	Geometry and orientation	Figure
<p>Shear failure shallow breakout</p> $\sigma_a > \sigma_{\theta\theta} > \sigma_{rr}$	<p>The failure will occur in the radial or axial plane because the maximum (σ_a) and minimum (σ_{rr}) stresses are oriented in a vertical plane</p>	
<p>Shear failure wide breakout</p> $\sigma_{\theta\theta} > \sigma_a > \sigma_{rr}$	<p>The failure will occur in the radial-tangential plane because the maximum ($\sigma_{\theta\theta}$) and minimum (σ_{rr}) stresses are oriented in the horizontal plane.</p>	
<p>Shear failure high-angle echelon</p> $\sigma_a > \sigma_{rr} > \sigma_{\theta\theta}$	<p>The failure will occur in the radial-tangential plane because maximum (σ_a) and minimum ($\sigma_{\theta\theta}$) stresses are oriented in the arc of the borehole wall.</p>	
<p>Shear failure narrow breakout</p> $\sigma_{rr} > \sigma_a > \sigma_{\theta\theta}$	<p>The failure will occur in the radial-tangential plane because the maximum (σ_{rr}) and minimum ($\sigma_{\theta\theta}$) stresses are oriented in the horizontal plane.</p>	

<p>Shear failure deep breakout</p> $\sigma_{rr} > \sigma_{\theta\theta} > \sigma_a$	<p>The failure will occur in the radial-axial plane because the maximum (σ_{rr}) and minimum (σ_a) stresses are oriented in a vertical plane.</p>	
<p>Shear failure low angle echelon</p> $\sigma_{\theta\theta} > \sigma_{rr} > \sigma_a$	<p>The failure will occur in the axial-tangential arc because the maximum ($\sigma_{\theta\theta}$) and minimum (σ_a) stresses are oriented in the arc of the borehole wall.</p>	

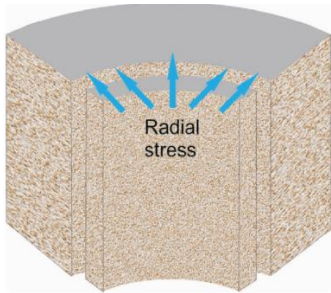
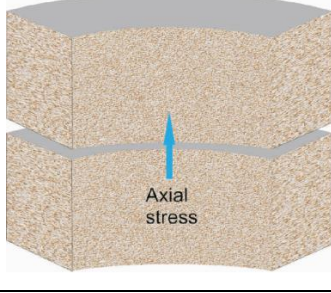
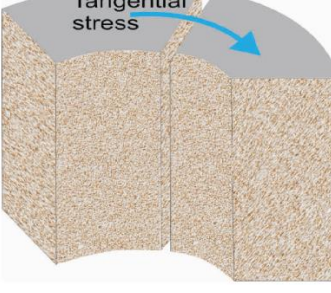
5.2 Borehole tensile failure

Tensile failure occurs when the least effective principal stress surpasses the formation rock tensile strength. Mathematically this can be expressed by Equation 10.

$$\sigma_3 \leq T_0 \tag{10}$$

Usually, tensile failure is produced by the extremely excessive weight of drilling mud, which results in massive mud circulation losses. Therefore, this failure becomes the upper limit of the mud density window in safe drilling practice. It is important to note here that the tensile strength of the rock can often be assumed to be zero because, theoretically, fractures can initiate in even small existing flaws (joints, fractures or faults). Tab. 2 explains the different modes of tensile failure.

Tab. 2. Modes of tensile failure in a borehole (after Pašić et al., 2007)

Failure type	Geometry and orientation	Figure
<p>Tensile Failure Cylindrical</p> $\sigma_{rr} < -T_0$	<p>This failure is concentric with the borehole.</p>	 <p>The diagram shows a cross-section of a borehole in a rock. Blue arrows point radially inward from the borehole wall, labeled 'Radial stress'. The failure is represented by a shaded cylindrical shell concentric with the borehole.</p>
<p>Tensile Failure Horizontal</p> $\sigma_a < -T_0$	<p>This failure creates horizontal fractures.</p>	 <p>The diagram shows a cross-section of a borehole in a rock. A blue arrow points vertically upward from the borehole wall, labeled 'Axial stress'. The failure is represented by horizontal shaded layers across the rock.</p>
<p>Tensile Failure Vertical</p> $\sigma_{\theta\theta} < -T_0$	<p>This failure creates a vertical fracture parallel to the maximum horizontal stress direction.</p>	 <p>The diagram shows a cross-section of a borehole in a rock. A blue arrow curves tangentially along the borehole wall, labeled 'Tangential stress'. The failure is represented by a vertical shaded fracture parallel to the maximum horizontal stress direction.</p>

6 Micro-mechanism of borehole breakout in different rocks

The borehole breakout mechanism can be divided into three phases:

- i) Phase 1: Initiation of breakout
- ii) Phase 2: Propagation of breakout
- iii) Phase 3: Extent and limit of breakout

Each of these three phases has specific characteristics and can be recognized independently. In the following, they are discussed in detail with examples of commonly drilled rocks: granite, limestone, and sandstone.

6.1 Borehole breakout in granite

Granite is an igneous intrusive rock of considerable strength. It consists mostly of quartz and feldspar grains visible to the naked eye which are accompanied by one or more dark minerals (ASTM C615 / C615M-11). In granite, the breakouts are initiated before the occurrence of any noticeable failure at the borehole surface. Under stresses, transgranular microcracks subparallel to the σ_{Hmax} direction develop just behind the borehole wall, as shown in the red circle in fig. 7. It is important to note here that in the beginning, these cracks do not have any effect on the wall of the borehole. Fig. 7 is taken and modified from Haimson (2007) who drilled a borehole in a granitic rock block and observed the

produced breakout. It shows that the micro-cracks develop (subparallel to σ_{Hmax}) just behind the wall of the borehole. It is also clear from this figure that despite the microcracks, the borehole wall is still intact. Since they do not show any shear offset, these cracks are dilatant and extensile.

In the second stage, the length and density of microcracks increase significantly. They form a multitude of thin columns following the path of least resistance. At this stage, the wall of the borehole starts to de-shape as shown in fig. 8. The rock flakes nearest to the borehole wall confront the highest end stresses and it buckles to the point of rupture at some critical magnitude,—with parts of it falling down into the borehole, leading to the breakout. The spalling of the first flake opens the way for the next flake to follow the path. The buckling and spalling process continues sequentially, which ultimately produces the breakout.

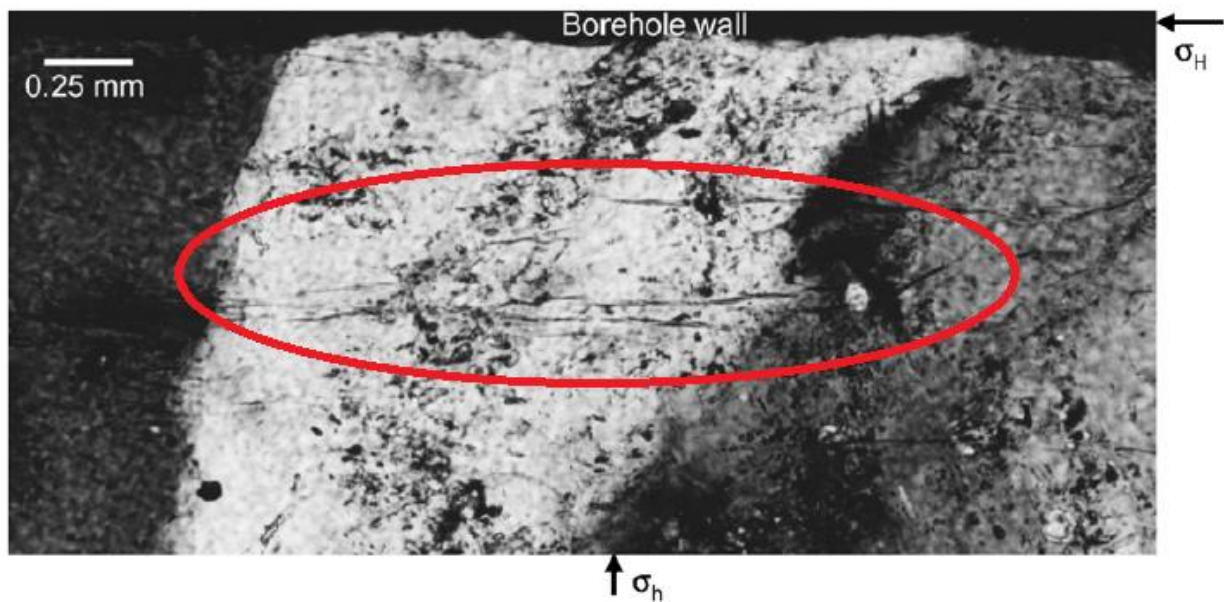


Fig. 7: Microcracks (inside red circle) behind the still visually undamaged borehole wall (modified after Haimson 2007).

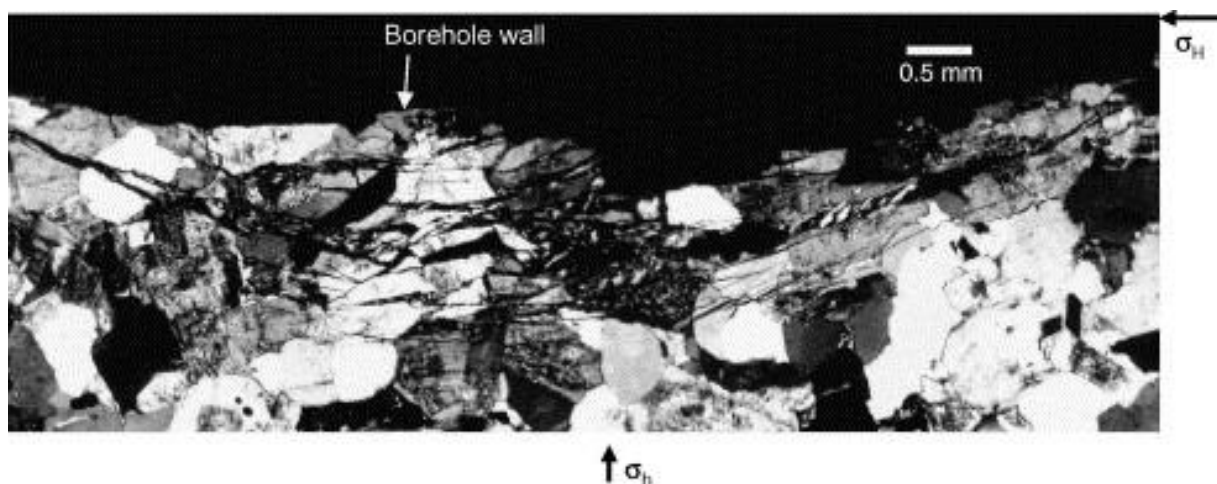


Fig. 8: Cluster of microcracks (Haimson, 2007).

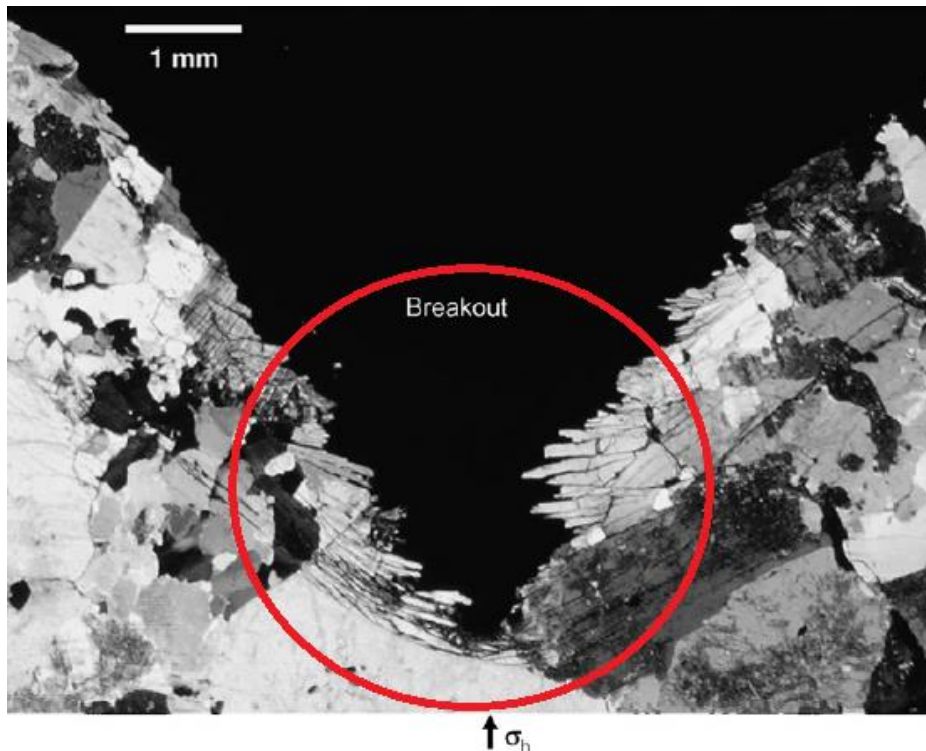


Fig. 9: Buckled and sheared-off rock flakes forming a V-shape breakout (modified after Haimson, 2007).

In the third phase, the breakout deepens in the direction of σ_{hmin} . The spalled flakes become shorter and shorter, causing the breakout span to become continuously narrower. This process ends when the next rock flake in succession is strong enough to withstand the stresses. This phenomenon causes a typical type of breakouts known as the V-shape breakout or dog-ear breakout (fig. 9).

6.2 Borehole breakout in limestone

As the mechanical properties of both, hard limestone and soft limestone differ greatly, the mechanism of borehole breakouts in both limestones differs consequently. However, both of these give rise to dog-ear shaped breakouts (same as in granites). The mechanism (three stages) of the development of a breakout in soft limestone is described in fig. 10. The breakout starts with the initiation of cracking along the grains of limestone (fig. 10(a)). These cracks develop in layers which result in the onset of borehole deformation, where cracks immediate to the borehole wall can easily be seen. In the next phase, i.e. the propagation of breakout, the existing cracks start to fail in shear (fig. 10(b)). In soft limestone, these shear cracks sometimes even have gouge or pieces of crushed rocks at the shear plane as shown in fig. 10(b). These shear cracks advance (during phase 3) into the rock following the high shear stress trajectories that ultimately form a dog-ear shaped breakout as shown in fig. 10(c).

It is interesting to note that contrary to the hard limestone, at phase 1 in soft limestone, extensional micro cracks (sub-parallel to σ_{Hmax}) are generated. Although hard limestone like the granite also has high unconfined compressive strength (UCS) but unlike the granite, the cracks in hard limestone are both inter- and intra-granular and extensional (in case of soft limestone shear cracks form). The tips of the cracks tilt toward the borehole. During this phase, the wall of the borehole remains unaffected, as was the case for granite above.

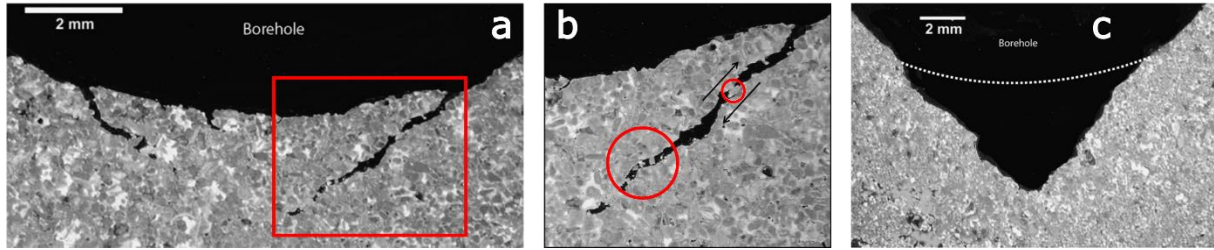


Fig. 10: Pictures showing the development of breakout in soft limestone: a) Dilatant shear crack, this crack advances into the rock along high shear stress trajectories, b) Two small circles show the gouge and crushed rock pieces in the shear plane, c) V-shaped breakout (modified after Haimson, 2007).

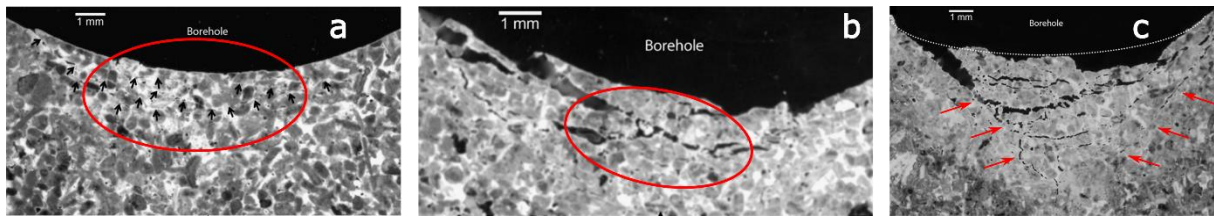


Fig. 11: Pictures showing the development of the breakouts in hard limestone: a) Immediate to the borehole, flakes are produced whereas the wall of the borehole is still undamaged (phase 1), b) Extensional micro cracks which deepen the borehole breakouts, c) V-shaped breakout with broad edges. In the given figures, the directions of stresses are as follows: σ_{Hmax} left – right, σ_{Hmin} bottom - top (modified after Haimson, 2007).

In the second phase, the rock flakes created by the cracks form sequentially and fall into the borehole which deepens the breakout. It is important to note that the crack between the grains follows the path of least resistance. In its last phase i.e. phase 3, the flakes strong enough to withstand the stress limit the extent of a breakout. As mentioned above, similar to the breakout in granites, the breakouts in hard limestone are also V-shaped. But their edges are broader in hard limestone whereas the edges are sharp in granite and soft limestone. The complete sequence of all the phases of breakout production in hard limestone is shown in fig. 11.

6.3 Borehole breakout in highly porous and quartz-rich sandstone

Like all breakouts, the breakouts in highly porous and quartz-rich sandstones also develop along σ_{Hmin} . However, their outstanding characteristic is their tabular shape which is long and narrow. This sometimes resembles hydraulic fractures. In laboratory experiments, it is observed that the length of the slot-shaped breakout is directly proportional to the diameter of the borehole. If we scale the lengths of the slot-shaped breakouts developed in the laboratory to oil-field well, it is not unimaginable that they could reach several meters. Micromechanically, slot-shaped breakouts are produced almost exclusively through the debonding of grains along σ_{Hmin} . It is also important to note that just ahead of the tip of slot-shaped breakouts, due to the accumulation of broken or crushed pieces, the porosity significantly reduces. Fig. 12 and fig. 13 show the slot-shaped breakout and breakout tip exposing the narrow zone of crushed grains which reduces the porosity.

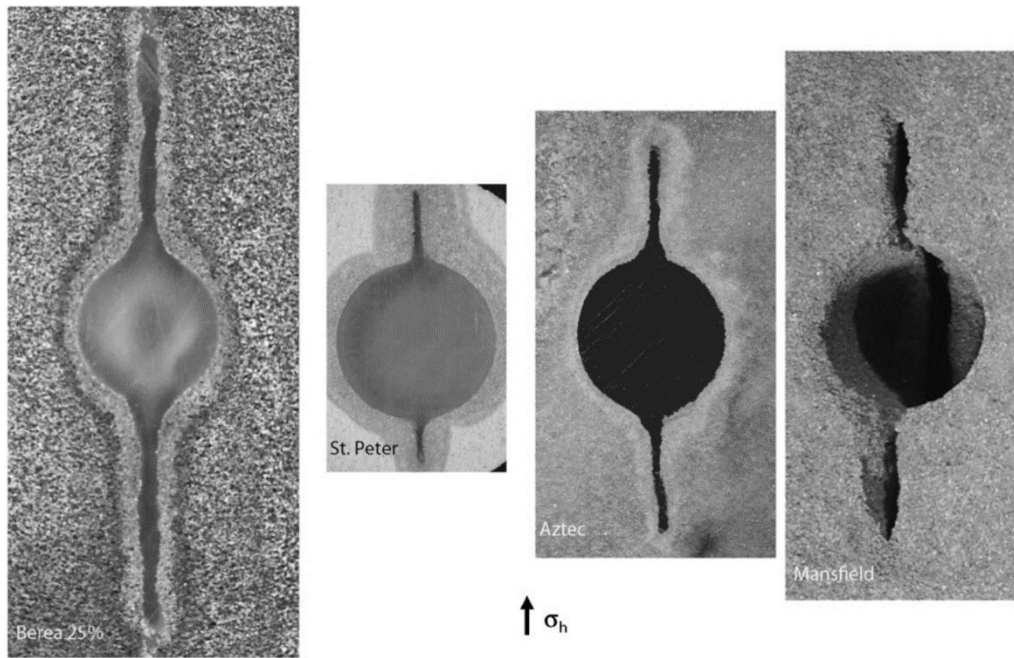


Fig 12: Slot-shaped borehole breakouts (Haimson, 2007).

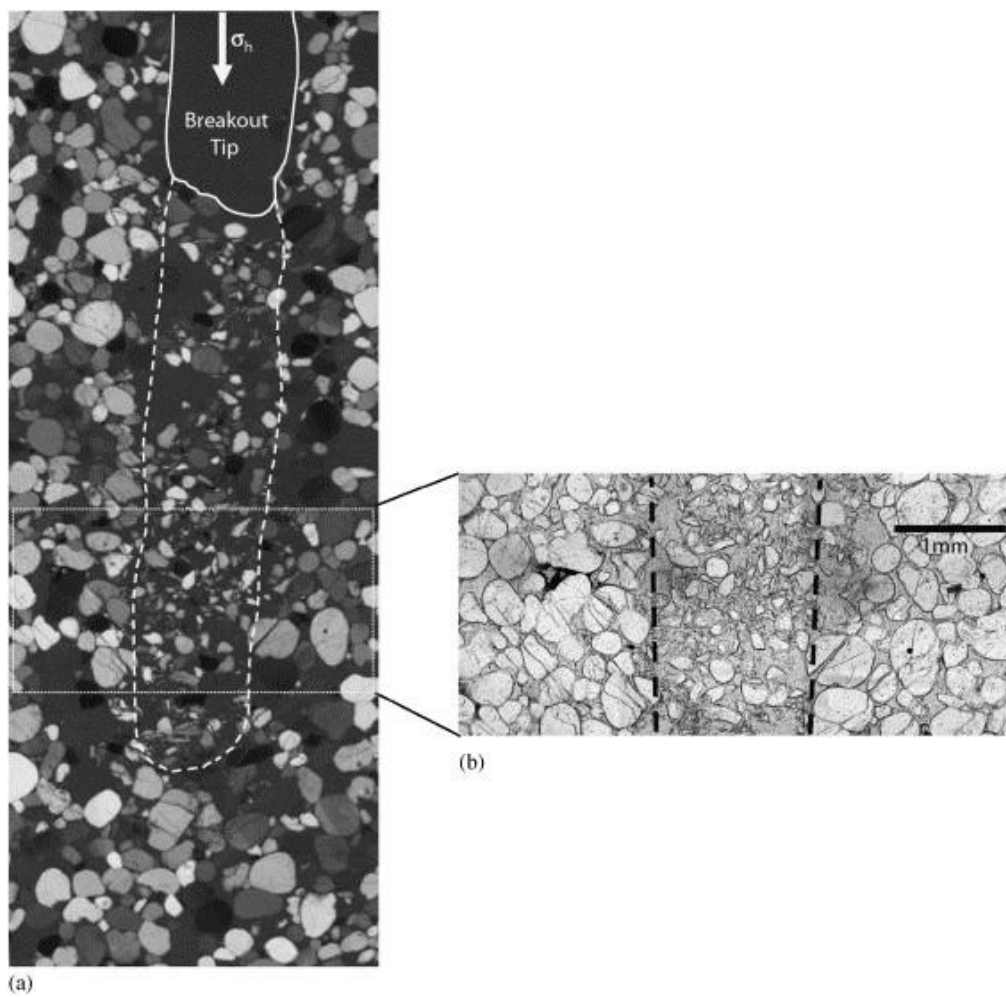


Fig. 13: a) Polarized light image of a slot-shaped breakout; b) image exposing the narrow zone of crushed grains that reduces the porosity (Haimson, 2007).

7 Rock strength anisotropy and borehole breakouts

The presence of weak bedding has a significant effect on the strength of the rocks. The effect of weak bedding planes lead to strength anisotropy. Rock strength anisotropy depends on the orientation of the plane with respect to the applied stresses and the relative weakness of the bedding planes. It is illustrated in Fig. 14(a) and Fig. 14(b) where the uniaxial compressive strength of the rock is plotted against different angles of bedding plane with respect to the applied stress.

It is clear from Fig. 14(b) that the strength of the rock decreases significantly when the angle between the applied stress and the bedding plane is 60° , whereas the rock demonstrates high strength when β is 0° and 90° . This anisotropy has also an effect on the borehole breakout. Vernik & Zoback (1990) hypothesized the formation of borehole breakouts in laminated rocks during the KTB project (Deep Continental Drilling Project, Germany). It was important to understand the mechanism of borehole breakout development in KTB as it was observed that there exist steeply dipping foliation planes cutting across the hole. In such cases, breakouts form due to two processes: i) when the stress concentration exceeds the intact rock strength (as in all the breakout processes) and ii) when the stress concentration activates movement on weak planes which further enlarges the failure zone. Contrary to V-shaped breakouts, double loop-shaped breakouts are produced in the presence of weak bedding planes as illustrated in fig. 15(a). In ultrasonic televiewer data, such a type of breakouts is recognized by the presence of four dark bands rather than two as in conventional breakouts (fig. 15(b)).

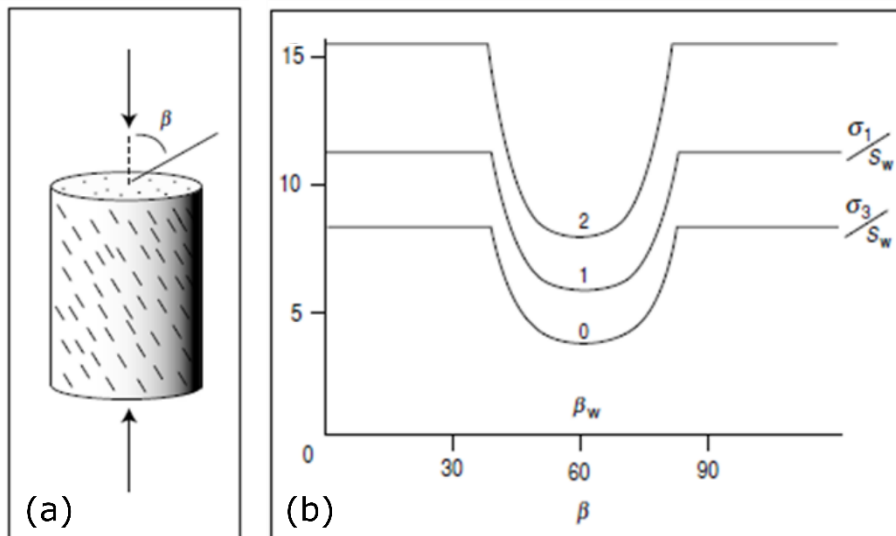


Fig. 14: a) Uniaxial compression test, angle β represents the relation of applied stress to bedding planes; b) Rock strength plotted against angle β , rock strength significantly decreases at about 60° (Zoback, 2007).

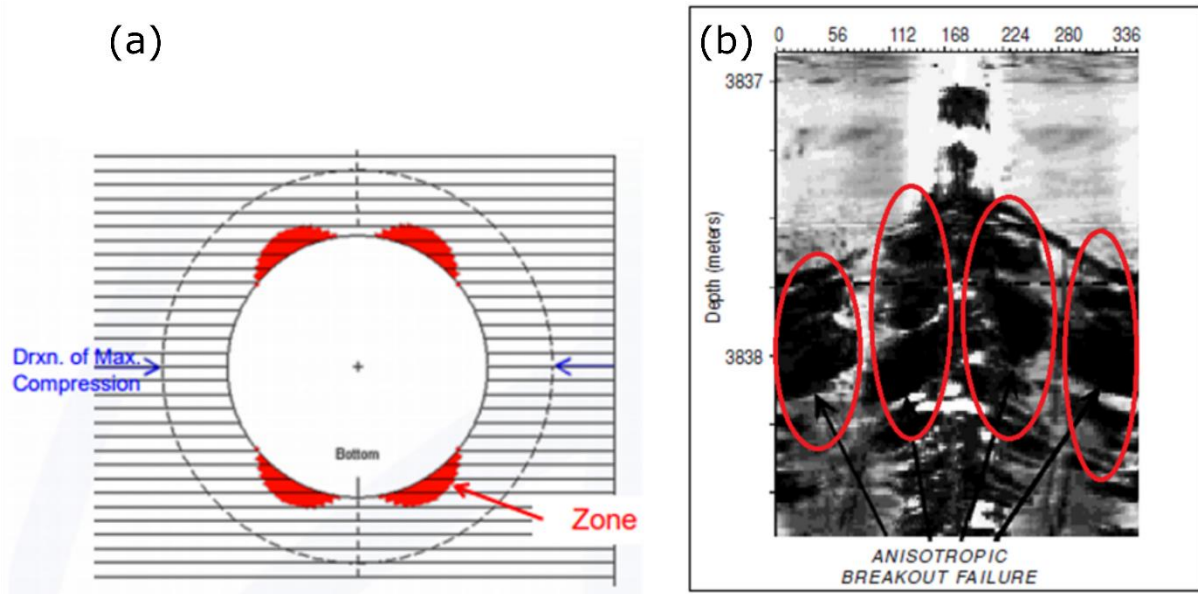


Fig. 15: a) Double loop-shaped borehole breakout, b) Four dark bands in the ultrasonic televiewer data showing the presence of double looped breakouts (Kowan & Ong, 2014; Zoback, 2007).

8 Estimating σ_{Hmax} from breakout

An accurate determination of σ_{Hmax} is very important in problems related to wellbore stability such as the determination of optimal mud weights, well trajectories, casing set points, etc. As discussed earlier, breakouts form around a wellbore when the stress concentration exceeds the rock strength. Once a breakout occurs, the circumferential stresses decrease thus preventing further widening of the breakout. Therefore, with the passage of time, the breakout will deepen but will not widen. This fact also leads to the assumption that just at the point where the breakout starts widening (maximum angle of breakout initiation), the strength of the rock and the stresses are in equilibrium, as shown in fig. 16.

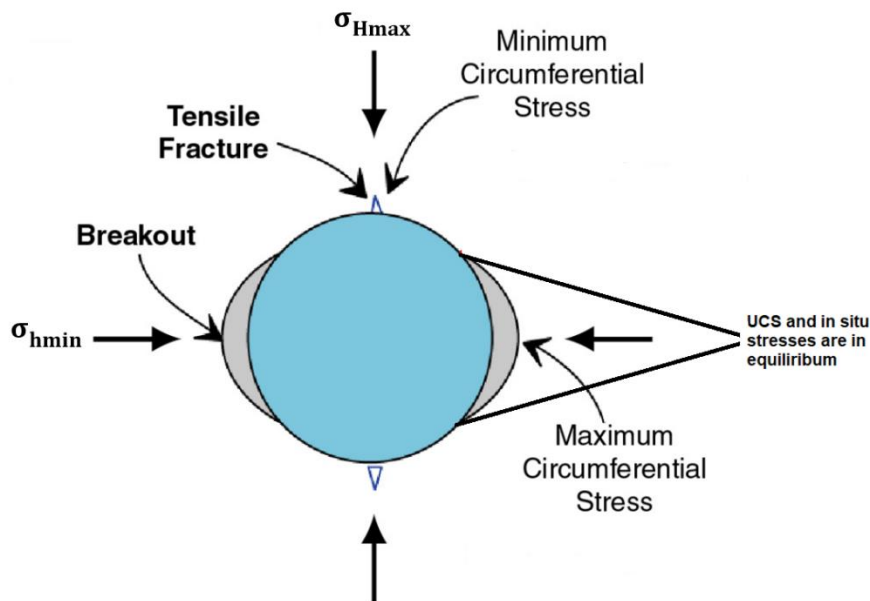


Figure 16: Sketch of borehole breakout showing the point where UCS and in situ stress are in equilibrium (modified after Smith et al., 2006)

With the assumptions that (i) the borehole width does not change as the breakout deepens and (ii) the breakout width corresponds to the azimuth at which the stress state first exceeds the rock strength and further assuming Mohr-Coulomb failure criterion, σ_{Hmax} may be estimated. Barton et al. (1988) and Townend & Zoback (2004) used this fact and proposed a methodology to determine σ_{Hmax} . Considering the two assumptions, the hoop stresses ($\sigma_{\theta\theta}$) given in equation 4 is equal to the UCS.

$$UCS = \sigma_{\theta\theta} = \sigma_1 + \sigma_3 - 2(\sigma_1 - \sigma_3)\cos(2\theta) \quad (11)$$

Using the effective stress law, where Biot-coefficient (α) is assumed to be 1 for brittle failure of intact rock (Nur and Byerlee, 1971), eq. (11) becomes

$$\sigma_{Hmax} = \frac{UCS + \Delta\sigma_{\theta\theta} - \sigma_{hmin}(1 + 2\cos(2\theta))}{1 - 2\cos(2\theta)} \quad (12)$$

Hence, with the known values of the pore pressure, the vertical stress, the least principal stress as well as a reasonable estimate of the rock strength (usually from the geophysical methods or laboratory measurements), and the observations of breakout width θ , one can determine the magnitude and direction of σ_{Hmax} . This technique has been successfully used in many parts of the world.

Another way to determine σ_{Hmax} is the so-called stress polygon shown in Fig. 17. The construction of the stress polygon is based on the Coulomb frictional sliding theory. According to this theory, the stress state is limited by the ratio between the two principal stresses (σ_1 and σ_3). If this ratio increases beyond certain values defined by the coefficient of friction (μ) of nearby faults, sliding occurs along critically oriented faults. Therefore, μ limits the stress state. The condition for Coulomb frictional sliding limit can be expressed by equations 13, 14 and 15 for normal faulting, strike slip faulting and reverse faulting, respectively.

$$\frac{\sigma_1}{\sigma_3} = \frac{\sigma_v - P_0}{\sigma_{hmin} - P_0} = \left(\sqrt{\mu^2 + 1} + \mu\right)^2 \quad \dots \text{ for normal faulting} \quad (13)$$

$$\frac{\sigma_1}{\sigma_3} = \frac{\sigma_{Hmax} - P_0}{\sigma_{hmin} - P_0} = \left(\sqrt{\mu^2 + 1} + \mu\right)^2 \quad \dots \text{ for strike slip faulting} \quad (14)$$

$$\frac{\sigma_1}{\sigma_3} = \frac{\sigma_{Hmax} - P_0}{\sigma_v - P_0} = \left(\sqrt{\mu^2 + 1} + \mu\right)^2 \quad \dots \text{ for reverse faulting} \quad (15)$$

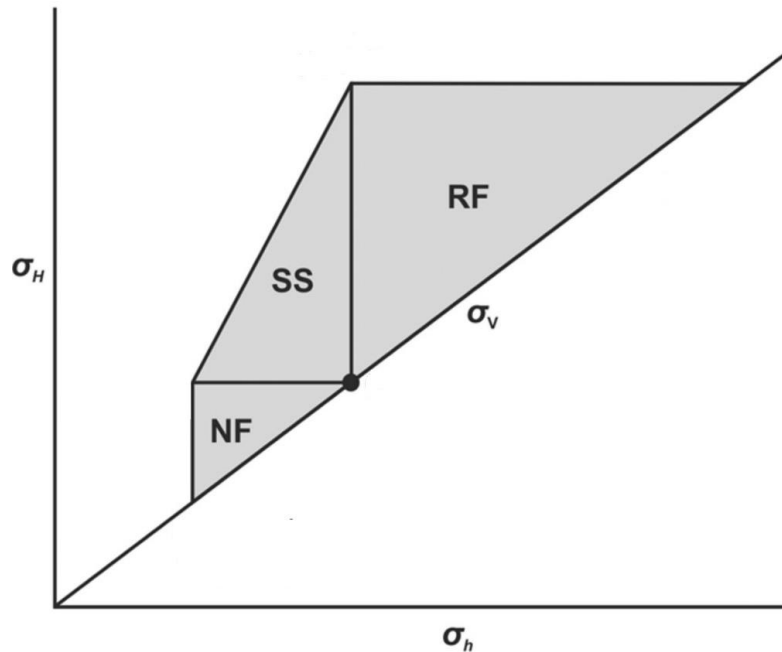


Fig. 17: Stress polygon (Zoback, 2007)

The equations for Coulomb frictional sliding can be plotted as three lines in the σ_{Hmax} versus σ_{hmin} diagram, as shown in fig. 17. This diagram is known as stress polygon. The stress polygon defines allowable values considering the two horizontal principal stresses for different structural regimes such as normal, strike slip, or reverse faulting. Outside the stress polygon, the rock would be at failure in its natural state. In order to estimate the stress through the stress polygon, the following data is necessary:

- Knowledge of structural regime (strike-slip faulting, normal faulting or reverse faulting),
- Vertical stress,
- Pore pressure,
- Magnitude of σ_{hmin} ,
- Width of the breakout,
- And strength of the rock (determined either from the lab testing or geophysical methods).

Fig. 18 shows two examples of stress estimation through stress polygon (Chang et al. 2010). In this study, the orientations and magnitudes of in-situ stresses are constrained using wall borehole breakouts and rock strength parameters. These boreholes were drilled in two different stress regimes and the necessary values to construct stress polygon, such as σ_v , breakout width, pore pressure, sliding friction, Poisson's ratio and internal friction were measured using different logging techniques and lab testing. These necessary values to construct the stress polygon are shown for each case. Fig. 18(a) and Fig. 18(b) estimate the value of σ_{Hmax} as dotted line and in the shaded area, respectively.

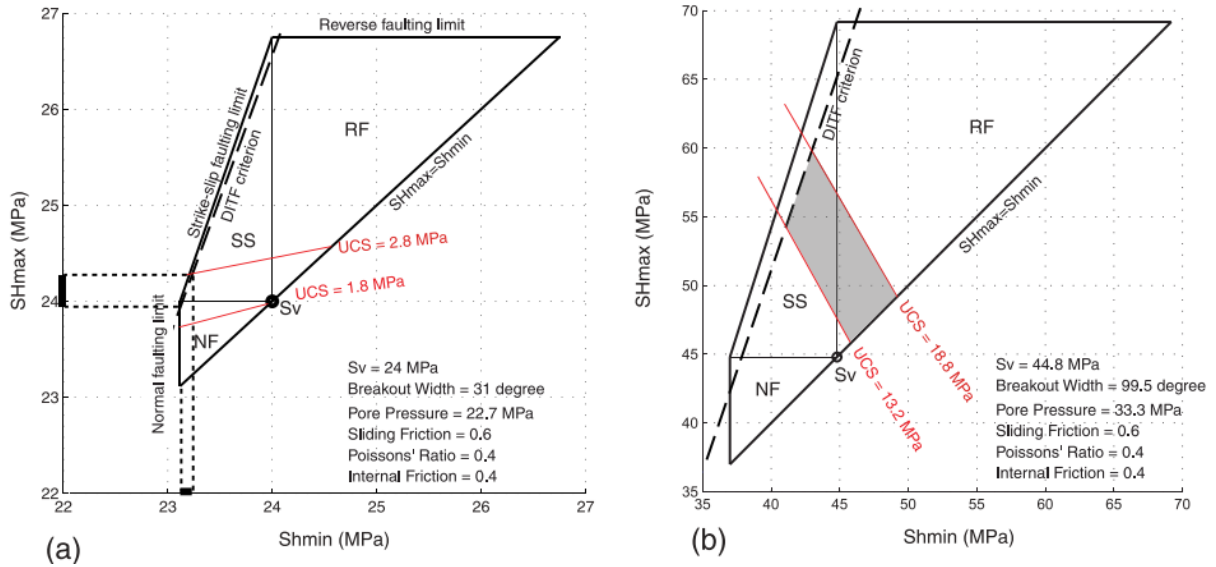


Fig. 18: Two examples of stress polygons showing information about the in-situ stresses and rock strength to estimate σ_{Hmax} (Chang et al., 2010).

9 Numerical modeling of borehole breakout

The elastic stress distribution around a borehole can be acquired analytically from the Kirsch equation, but there is no analytical solution available to predict the shape and time of borehole breakout. Therefore, numerical modeling approaches have to be applied. The numerical modeling documented in this chapter is aimed to illustrate borehole breakout in a selected geological regime. A 2D approach is selected to simulate the case, as the principal stresses are vertical and horizontal. An elasto-plastic strain-softening Mohr-Coulomb model using FLAC (version 7.0, Itasca Consulting Group) was applied. The values of the mechanical properties used in this study are listed in Table 4. Material parameters were calibrated on uniaxial and triaxial lab tests performed at different confining pressures (5 MPa, 10 MPa, 20 MPa and 30 MPa). Fig. 20(a) illustrates the shear bands in numerical simulations and Fig. 20(b) shows a comparison between lab test results and simulations.

Tab 4: Material parameters for numerical borehole breakout simulation with FLAC

Property, unit	Value
Shear Modulus, GPa	12
Bulk Modulus, GPa	20
Density, kg/m ³	2590
Friction, deg	55
Cohesion, MPa	20
Dilation angle, deg	10
Tensile strength, MPa	7

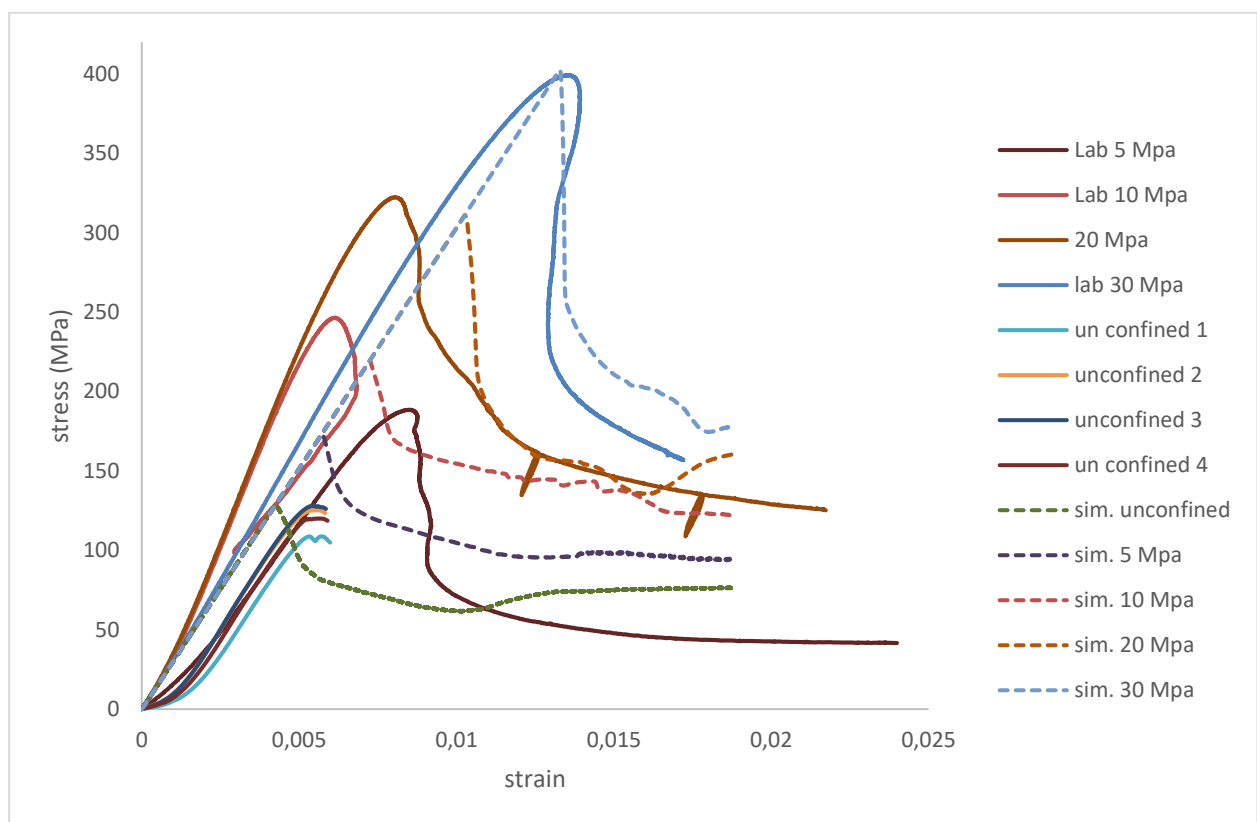
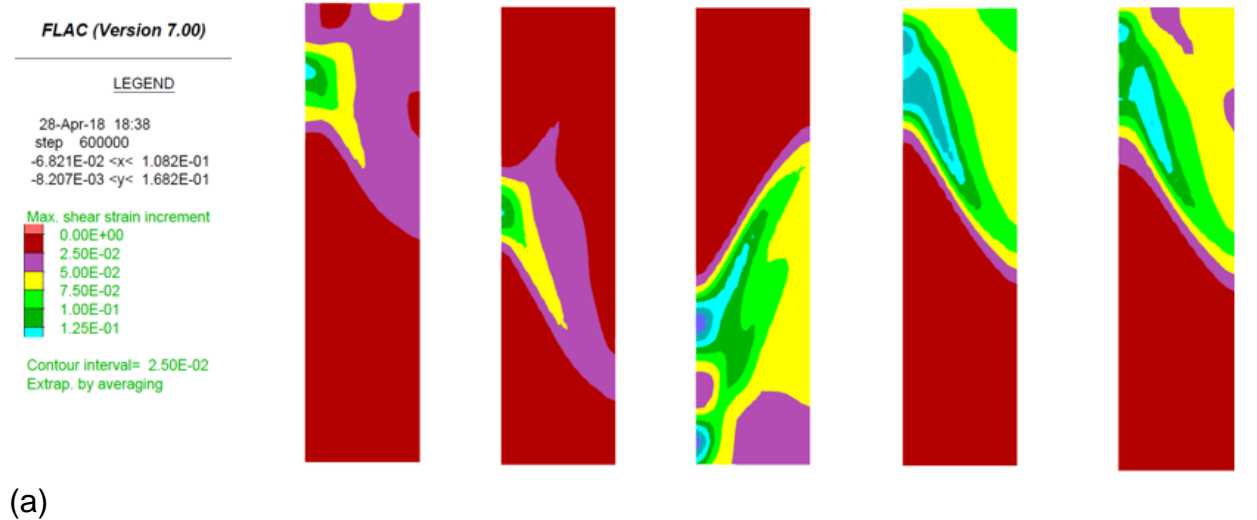


Fig 18: Simulation of triaxial lab tests: (a) shear bands observed in triaxial test simulations for confining pressures of 5, 10, 20 and 30 MPa; (b) stress-strain curves of laboratory tests and simulations (Sadiq & Konietzky, unpublished report)

Borehole breakouts are predicted numerically by adopting the following steps:

- 1) Set-up of numerical model including defining borehole geometry, rock properties, and in-situ stresses,
- 2) Running the model to equilibrium,
- 3) Analysing the areas around the borehole in detail (size, failure mode, etc.).

Different models were executed in which the magnitude of σ_v , σ_{Hmax} , and σ_{hmin} were changed. The stress ratio $\sigma_{Hmax}/\sigma_{hmin}$ varies between 0.25 to 2.5 and the ratio of σ_v/σ_{hmin} ranges from 0.5 to 2. The breakout angle is defined as the azimuth angle of the breakout at the borehole wall, whereas the breakout depth is defined as the distance between the tips of the breakout to the original borehole wall, as illustrated in fig. 19. Fig. 20 shows selected results obtained from the numerical simulations. Several observations can be made based on these results:

- Breakouts are caused by the combined effect of tensile and shear fracturing. The failure initiates at the borehole wall and then propagates into the rock.
- For a given σ_{Hmax} , lower σ_{hmin} results are gained in a deeper breakout. It implies that the depth of the breakout is dependent on the stress ratio $\sigma_{Hmax}/\sigma_{hmin}$. Fig. 21 shows the variation of the depth of borehole breakout modeled.
- For a given σ_{hmin} , a higher σ_{Hmax} will result in a wider breakout. It implies that the width (also known as azimuth angle) of the breakouts depends on the magnitude of the major horizontal principal stress. Fig. 22 shows the variation of the width of the modelled borehole breakout.

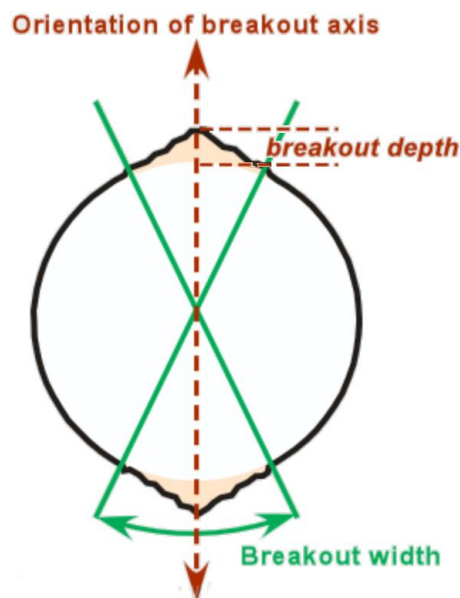


Fig. 19: Sketch of breakout width and depth (modified after Lacazett, 2017).

FLAC (Version 7.00)

LEGEND

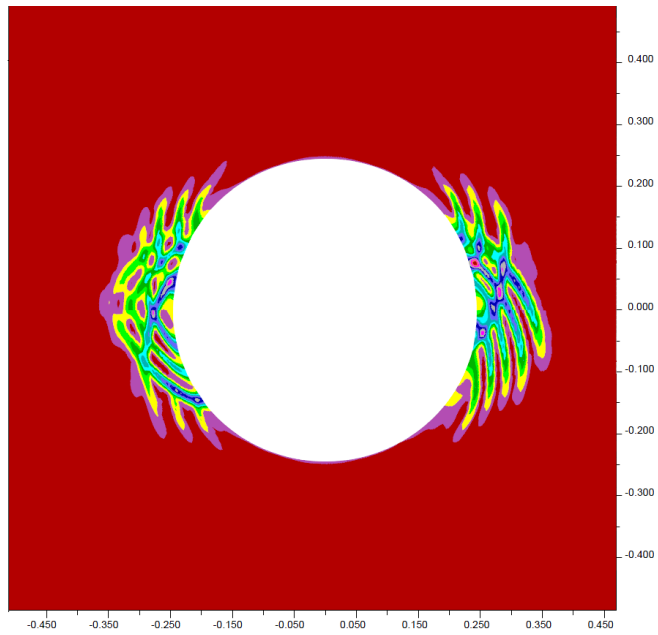
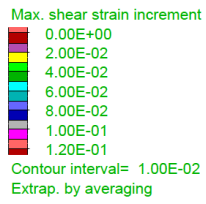


Fig. 20: Modeled borehole breakouts using FLAC, showing shear strain increments (Sadiq & Konietzky, 2018)

10 Nomenclature

$\sigma_1, \sigma_2, \sigma_3$	= Principal stresses
σ_v	= vertical stress
σ_{Hmax}	= Maximum horizontal stress
σ_{hmin}	= Minimum horizontal stress
$\sigma_{\theta\theta}$	= Circumferential or hoop stresses
σ_{rr}	= Radial stress
σ_a	= Axial stress
ν	= Poisson's ratio
P_0	= Hydraulic borehole pressure
R	= Radius of borehole
UCS	= Unconfined compressive strength

Note: all stresses are effective stresses (= total stress - pore water pressure)

11 References

- Lacazett, A. (2017). Breakouts and Induced Fracture Basics: Don't make these common mistakes, *Al Lacazett's NaturalFractures.com*, <http://www.naturalfractures.com/3.1.htm>, last accessed: 23.08.2018.
- Aslannezhad, M., Khaksar manshad, A. & Jalalifar, H. (2016). Determination of a safe mud window and analysis of wellbore stability to minimize drilling challenges and non-productive time. *Journal of Petroleum Exploration and Production Technology*, 6(3), 493–503.
- Asquith, G.B. & Krygowski, Daniel (2004). Basic well log analysis. Tulsa: American Assoc. of Petroleum Geologists (AAPG methods in exploration series, 16).
- ASTM C615 / C615M-11, Standard Specification for Granite Dimension Stone, ASTM International, West Conshohocken, PA, 2011, www.astm.org
- Awal, M. R., Khan, M. S., Mohiuddin, M. A., Abdulraheem, A. & Azeemuddin, M. (2001). A New Approach to Borehole Trajectory Optimisation for Increased Hole Stability. Society of Petroleum Engineers, SPE Middle East Oil Show, 17-20 March, Manama, Bahrain.
- Barton, C. A., Zoback, M. D. & Burns, K. L. (1988). In-Situ Stress Orientation and Magnitude at the Fenton geothermal site, New Mexico, determined from wellbore breakouts. *Geophysical Research Letters*, 15(5), 467–470.
- Bell, J. S. & Babcock, E. A. (1986). The stress regime of the Western Canadian Basin and implications for hydrocarbon production. *Bulletin of Canadian Petroleum Geology*, 34, 364–378.
- Bell, J. S. & Gough, D. I. (1979). Northeast-southwest compressive stress in Alberta: Evidence from oil wells. *Earth Planet. Sci. Lett.*, 45, 475–482.
- Bell, J.S., Price, P.R. & McLellan, P.J. (1994). In-situ Stress in the Western Canada Sedimentary Basin; In: Geological Atlas of the Western Canada Sedimentary Basin, G.D. Mossop and I. Shetsen (comp.), Canadian Society of Petroleum Geologists and Alberta Research Council, https://ags.aer.ca/image-content/fg29_02.jpg, last accessed: 21.08.2018.

- Bird, P. (2003). An updated digital model of plate boundaries. *Geochemistry, Geophysics, Geosystems*, 4(3), 1027.
- Bratton, T., Bornemann, T., Li, Q., Plumb, R., Rasmus, J., & Krabbe, H. (1999). Logging-while-drilling images for geomechanical, geological and petrophysical interpretations. 40th Annual Logging Symposium, SPWLA, Expanded Abstracts.
- Chang, C., McNeill, L. C., Moore, J. C., Lin, W., Conin, M. & Yamada, Y. (2010). In situ stress state in the Nankai accretionary wedge estimated from borehole wall failures. *Geochemistry, Geophysics, Geosystems*, 11(12), 1–17.
- Cox, J. W. (1970). The high resolution dip-related borehole and formation characteristics, Society of Professional Well log Analysts, 11th Annual Logging Symposium, Los Angeles.
- David, C. & Le Ravalec-Dupin, M. (2007). Rock Physics and Geomechanics in the Study of Reservoirs and Repositories. *Geological Society, London, Special Publications*, 284, 1–14.
- Haimson, B. (2007). Micromechanisms of borehole instability leading to breakouts in rocks, *International Journal of Rock Mechanics and Mining Sciences*, 44(2), 157–173.
- Heidbach, O., Tingay, M., Barth, A., Reinecker, J., Kurfeß, D. & Müller, B. (2010). Global crustal stress pattern based on the World Stress Map database release 2008. *Tectonophysics*, 482(1–4), 3–15.
- Kim, H., Xie, L., Min, K.-B., Bae, S. & Stephansson, O. (2017). Integrated In Situ Stress Estimation by Hydraulic Fracturing, Borehole Observations and Numerical Analysis at the EXP-1 Borehole in Pohang, Korea. *Rock Mechanics and Rock Engineering*, 50(12), 3141-3155
- Kirsch, E.G. (1898). Die Theorie der Elastizität und die Bedürfnisse der Festigkeitslehre, *Zeitschrift des Vereines deutscher Ingenieure*, 42, 797–807.
- Klein, R. J. & Barr, M. V. (1986). Regional state of stress in western Europe. *Proceedings of the International Symposium on Rock Stress and Rock Stress Measurement*. Stockholm, 1-3 september 1986, 33–44.
- Kowan, J. & Ong, S. H. (2014). Well bore stability: Special consideration for the Marcellus Shale. Geoscience Technology Workshop, Pittsburgh Pennsylvania.
- Leeman, E. R. (1964). The measurement of stress in rock - part I: the principles of rock stress measurements. *Journal of the South African Institute of Mining and Metallurgy*, 65(2), 45–81.
- McLean, M. R. & Addis, M. A. (1990). Wellbore Stability Analysis: A Review of Current Methods of Analysis and Their Field Application, Society of Petroleum Engineers, SPE/IADC Drilling Conference, 27 February - 2 March, Houston, Texas
- Meier, T., Rybacki, E., Reinicke, A. & Dresen, G. (2013). Influence of borehole diameter on the formation of borehole breakouts in black shale, *International Journal of Rock Mechanics and Mining Science*, 62, 74-85.
- Mount, V. S. & Suppe, J. (1987). State of stress near the San Andreas fault: Implications for wrench tectonics. *Geology*, 15(12), 1143–1146.

- Nur, A. & Byerlee, J. (1971). An effective stress law for elastic deformations of rock with fluids. *J. Geophys. Res.*, 76, 6414–6419.
- Pašić, B., Gaurina-Međimurec, N. & Matanović, D. (2007). Wellbore Instability: Causes and consequences. *Rudarsko-geološko-naftni zbornik*, 19, 87–98.
- Plumb, R. A. & Cox, J. W. (1987). Stress directions in eastern North America determined to 4.5 km from borehole elongation measurements. *Journal of Geophysical Research*, 92, 4805–4816.
- Plumb, R. & Hickman, S. H. (1985). Stress-induced borehole elongation : A comparison between the four-arm dipmeter and the borehole televiewer in the Auburn. *Journal of Geophysical Research*, 90(B7), 5513–5521.
- Reinecker, J., Tingay, M. & Müller, B. (2003). Borehole breakout analysis from four arm caliper logs. Guidelines: Four-arm Caliper Logs, World Stress Map Project , http://dc-app3-14.gfz-potsdam.de/pub/guidelines/WSM_analysis_guideline_breakout_caliper.pdf, last accessed: 21.08.2018
- Sadiq, R.A.B. & Konietzky, H. (2018), Numerical investigations of borehole breakout in Granite, unpublished report
- Shen, B. (2008). Borehole Breakouts and In Situ Stresses. In A. D. & R. J. Y Potvin, J Carter (Ed.), *Proceedings of the First Southern Hemisphere International Rock Mechanics Symposium* (pp. 407–418). Perth: Australian Centre for Geomechanics.
- Smith, S., Ismail, I.Y., Brehm, A., & Castillo, D. (2006). Impact of Tectonic Stress Variation on Field Development Planning in The Temana and Bazan Fields, Sarawak Basin, GEO Asia 2006, Kuala Lumpur
- Tingay, M., Müller, B., Reinecker, J., Heidbach, O., Wenzel, F. & Fleckenstein, P. (2005). Understanding tectonic stress in the oil patch: The World Stress Map Project. *The Leading Edge*, 24(12), 1276–1282.
- Townend, J. & Zoback, M. D. (2004). Regional tectonic stress near the San Andreas fault in central and southern California. *Geophysical Research Letters*, 31(15), 1–5.
- Vernik, L. & Zoback, M. D. (1990). Strength anisotropy in crystalline rock: Implications for assessment of in situ stresses from wellbore breakouts, In: *Rock Mechanics Contributions and Challenges*, Balkema, Rotterdam, 841-848,
- Zoback, M. D. (2007). *Reservoir Geomechanics*, Cambridge: Cambridge University Press
- Zoback, M. D., Barton, C. A., Brudy, M., Castillo, D. A., Finkbeiner, T., Grollimund, B. R. & Wiprut, D. J. (2003). Determination of stress orientation and magnitude in deep wells. *International Journal of Rock Mechanics and Mining Sciences*, 40(7–8), 1049–1076
- Zoback, M. D., Moos, D., Mastin, L., & Anderson, R. N. (1985). Well bore breakouts and in situ stress. *Journal of Geophysical Research*, 90(B7), 5523.
- Zoback, M. L. (1992). First- and second-order patterns of stress in the lithosphere: The World Stress Map Project. *Journal of Geophysical Research*, 97(B8), 11703–11728.